Correlation between Structure and Magnetic Spin State of the Manganese Cluster in the Oxygen-Evolving Complex of Photosystem II in the S_2 State: Determination by X-ray Absorption Spectroscopy†

Wenchuan Liang,‡,§ Matthew J. Latimer,‡,§ Holger Dau,‖ Theo A. Roelofs,‡,§ Vittal K. Yachandra,*,‡ Kenneth Sauer,*,‡,§ and Melvin P. Klein*,‡

Department of Chemistry and Structural Biology Division, Lawrence Berkeley Laboratory, University of California, Berkeley, California 94720

Received December 8, 1993; Revised Manuscript Received February 23, 1994⊕

ABSTRACT: The structure of the manganese cluster in the S_2 state with the $g \approx 4$ EPR signal (S_2-$g4$ state) generated by 130 K illumination of photosystem II (PSII) membranes prepared from spinach has been investigated by X-ray absorption spectroscopy. The Mn X-ray absorption K-edge spectra of the S_2-$g4$ state not only show a shift of the inflection point to higher energy from the S_1 state but also reveal a different edge shape from that of the S_2 state with the multiline signal (S_2-MLS state). Extended X-ray absorption fine structure (EXAFS) studies of the Mn K-edge show that the structure of the Mn cluster in the S_2-$g4$ state is distinctly different from those in the S_2-MLS or S_1 states. In the S_2-$g4$ state, the second shell of back-scatterers from the Mn absorber is found to contain two Mn–Mn distances of 2.73 and 2.85 Å. We interpret this to indicate the presence of two nonequivalent di-μ-oxo-bridged Mn binuclear structures in the Mn cluster of the S_2-$g4$ state. The third shell of the S_2-$g4$ state at about 3.3 Å also contains increased heterogeneity. By contrast, very little distance disorder was found to exist in the second shell of the S_1 or S_2-MLS states. A mechanism is proposed to explain these results in the context of our model for the Mn cluster and the EPR properties of the Mn complex in the S_2 state.

The oxygen-evolving complex (OEC[1]) of the photosystem II (PSII) reaction center of plants and cyanobacteria catalyzes the oxidation of two water molecules to one molecule of dioxygen. To couple the four-electron oxidation of water with the one-electron photochemistry occurring at the PSII reaction center, a manganese cluster in the OEC is thought to cycle through five intermediate states, S_i (i = 0, ..., 4), with i representing the number of oxidative equivalents stored in the OEC (Kok et al., 1970). In long-term (tens of minutes) dark-adapted samples, the S_1 state predominates. The S_4 state is believed to be a transient intermediate that spontaneously returns to the S_0 state with the release of one molecule of dioxygen. Ca^{2+} and Cl^- ions are essential cofactors for oxygen evolution activity. The roles of these two essential cofactors, the structure of the Mn cluster in the OEC, the mechanism of charge storage, and the oxidation of water to molecular oxygen have been the subject of intensive study [reviewed in Rutherford (1989, 1992); Debus, 1992].

Two low-temperature electron paramagnetic resonance (EPR) signals have been assigned to the Mn cluster in the S_2 state, on the basis of the observed oscillation amplitudes of these signals from samples advanced through the S states with short flashes of light. The multiline signal (MLS) centered at g = 2, exhibiting at least 18 partially resolved hyperfine lines at X-band (~9 GHz), is suggestive of the presence of an exchange-coupled cluster of at least two Mn atoms (Dismukes & Siderer, 1981; Hansson & Andréasson, 1982). The second signal attributed to the Mn cluster in the S_2 state is centered at $g \approx 4$ with a peak-to-peak separation of 32–36 mT (denoted S_2-$g4$ signal) and does not exhibit resolved hyperfine features (Casey & Sauer, 1984; Zimmermann & Rutherford, 1984) except under certain conditions (see below). This S_2-$g4$ signal, like the MLS, has been shown to arise from an active form of the Mn cluster, on the basis of similar abilities to convert the S_2 to the S_3 state and ultimately produce oxygen (Ono et al., 1987; Andréasson, 1990; Haddy et al., 1990). Conclusive assignment of the S_2-$g4$ signal to a multinuclear Mn cluster was made upon the observation of at least 16 resolved Mn hyperfine lines on the $g \approx 4$ EPR signal from oriented ammonia-treated PSII preparations (Kim et al., 1990).

The relative amplitudes of the two S_2 EPR signals are sensitive to a variety of experimental conditions. In samples illuminated at 200 K, both signals are observed in the presence of sucrose, while with glycerol, ethylene glycol, or ethanol, only the MLS appears (Zimmermann & Rutherford, 1986; De Paula et al., 1987). However, at lower illumination temperature (130–140 K), the S_2-$g4$ EPR signal appears predominantly. Annealing the S_2-$g4$ samples to 200 K in the dark generates more MLS at the expense of the $g \approx 4$ EPR

† This work was supported by grants from the National Science Foundation (DMB91-04104) and by the Director, Division of Energy Biosciences, Office of Basic Energy Sciences, Department of Energy, under contract DE-AC03-76SF00098. Synchrotron radiation facilities were provided by the Stanford Synchrotron Radiation Laboratory (SSRL) and the National Synchrotron Light Source (NSLS), both supported by the U.S. Department of Energy. The Biotechnology Laboratory at SSRL and beam line X9-A at NSLS are supported by the National Center for Research Resources of the National Institutes of Health.

* Authors to whom correspondence should be addressed.

‡ Structural Biology Division.

§ Department of Chemistry.

‖ Present address: Fachbereich Biologie/Botanik, Philipps-Universität Marburg, Lahnberge, D-35032 Marburg, Germany.

⊕ Abstract published in *Advance ACS Abstracts,* April 1, 1994.

[1] Abbreviations: Chl, chlorophyll; EPR, electron paramagnetic resonance; EXAFS, extended X-ray absorption fine structure; MES, 2-morpholinoethanesulfonic acid; MLS, multiline EPR signal; OEC, oxygen-evolving complex; PSII, photosystem II; Q_A, a plastoquinone electron acceptor of the PSII reaction center; S_2-$g4$ state, the S_2 state with the g = 4 EPR signal; S_2-MLS state, the S_2 state with the MLS signal; S_2-ann. sample, annealed S_2-$g4$ sample; XAS, X-ray absorption spectroscopy.

0006-2960/94/0433-4923$04.50/0

signal (Casey & Sauer, 1984). PSII preparations treated with NH_3, F^-, NO_3^-, or I^- or when Ca^{2+} is replaced by Sr^{2+} have been reported to show an enhanced S_2-$g4$ signal (Casey & Sauer; 1984; Beck & Brudvig, 1986, 1988; Ono et al., 1987; Boussac & Rutherford, 1988; Ono & Inoue, 1989; DeRose, 1990). Not all of the S_2-$g4$ signals mentioned above have the same line widths and g-values. The two species characterized by the two S_2 signals have been proposed to be interrelated, on the basis of the observation of the amplitude conversion of S_2-$g4$ to S_2-MLS (Zimmermann & Rutherford, 1986; Beck & Brudvig, 1986; Hansson et al., 1987). Recent EPR measurements strongly support a model in which S_2-$g4$ and S_2-MLS arise from different spin-state configurations of an exchange-coupled tetranuclear Mn complex (Kim et al., 1992). It is known that the MLS originates from the $S = {}^1/_2$ ground state (Britt et al., 1992). On the other hand, multifrequency EPR studies provide evidence that the S_2-$g4$ signal originates from the middle Kramers doublet of a near-rhombic $S = {}^5/_2$ state (Haddy et al., 1992).

Investigation of the coordination chemistry of the Mn cluster is important to better understand the catalytic mechanism of water oxidation. We have used X-ray absorption spectroscopy to study the local structure of the Mn cluster in the OEC. Observation of a positive shift in the Mn X-ray K-edge energy provided direct evidence for the oxidation of Mn accompanying the S_1 to S_2-MLS transition (Goodin et al., 1984). Similar conclusions were reported on the basis of the Mn K-edge study of S_2-$g4$ samples measured at 170 K (Cole et al., 1987). Extended X-ray absorption fine structure (EXAFS) studies provide further information about the types of ligands, Mn to ligand distances, and coordination number of the Mn cluster (Yachandra et al., 1987). Extensive EXAFS studies have been performed to characterize the S_2-MLS and S_1 samples (DeRose, 1990; Penner-Hahn et al., 1990; Sauer et al., 1992; MacLachlan et al., 1992; Yachandra et al., 1993). However, no EXAFS studies on the S_2-$g4$ samples, either from native or treated PSII preparations, are available. The observation that at 130–140 K the native $g \approx 4$ EPR signal was generated predominantly, but converted to the MLS signal upon annealing at 200 K, has led to the suggestion that the molecular configuration of the Mn cluster in the S_2-$g4$ state is closer to that in the dark-adapted S_1 state (de Paula et al., 1987).

In this article, we present the results of Mn K-edge and EXAFS experiments performed on native PSII samples poised predominantly in the S_2-$g4$ state by illumination at 130 K. The X-ray absorption data presented here are of significantly improved quality compared with the Mn K-edges we reported earlier for the S_2-$g4$ samples (Cole et al., 1987), mainly due to the use of a 13-element Ge fluorescence detector and data collection at 10 K. Results presented here confirm our previous study of the S_2-$g4$ samples, indicating the oxidation of Mn in the advance from the S_1 to the S_2-$g4$ state. However, between the S_2-$g4$ and S_2-MLS samples, differences in the edge position and shape are now detected. Furthermore, the EXAFS analyses surprisingly showed an altered molecular configuration of the Mn cluster in the S_2-$g4$ state. This is unexpected, because our previous EXAFS results showed that the structure of the Mn cluster in the OEC remained substantially unchanged during the S_1 to S_2-MLS transition (DeRose, 1990; Sauer et al., 1992). Unlike the S_1 or S_2-MLS states, both the second and third shells of the Mn back-scatterers in the S_2-$g4$ state contain increased heterogeneity. Conclusions are drawn from a detailed comparison of the simulation results obtained from the S_1, S_2-MLS, S_2-$g4$, and S_2-ann. (S_2-ann.: S_2-$g4$ samples annealed in the dark at 200 K, which produces the S_2-MLS state) samples. The significance of these analyses and models for the Mn cluster of the OEC is discussed.

MATERIALS AND METHODS

Preparation of PSII Membranes. Oxygen-evolving PSII membranes from spinach were prepared using the BBY protocol (Berthold et al., 1981), with typical oxygen-evolution activity of 500–600 μmol of O_2/mg of Chl/h. The PSII membrane pellets were resuspended to a concentration of 2 mg of Chl/mL in medium A (15 mM NaCl, 5 mM $MgCl_2$, 5 mM $CaCl_2$, and 50 mM MES at pH 6.5) with 0.4 M sucrose and centrifuged for 30 min at 37000g. The pellets then were washed again in medium A with 50% glycerol as the cryoprotectant and centrifuged again. Chemical oxidation of cytochrome b_{559} was accomplished by incubating PSII membranes suspended at 3 mg of Chl/mL in the dark for 10 min at 4 °C in medium A with 5 mM $K_3W(CN)_8/K_4W(CN)_8$ and then washing and centrifuging as above.

The samples for X-ray absorption studies were prepared by mounting these PSII membrane pellets directly onto the lucite sample holders, with a hollowed compartment (dimensions of $2.1 \times 0.3 \times 0.15$ cm^3) backed by a piece of mylar tape. The other open side directly faced the incoming X-ray beam. All illuminations, EPR, and X-ray absorption measurements were performed directly on samples mounted in these holders. Chlorophyll concentrations in these samples ranged from 20 to 25 mg of Chl/mL.

Illumination and EPR Analysis. Samples prepared as described above were kept in the dark for 2 h at 4 °C to poise the PSII membranes in the S_1 state and then frozen in liquid nitrogen. Prior to illumination, samples were equilibrated for 2 min in an unsilvered dewar at 131 ± 3 K (for the S_2-$g4$ state) or 195 K (for the S_2-MLS state). Samples were continuously illuminated for 7 min using a 400-W tungsten lamp, with a 7-cm path of 5% aqueous $CuSO_4$ as a heat filter. The temperature was maintained at 195 K in a dry ice/methanol bath or at 131 ± 3 K with a continuous stream of liquid nitrogen-cooled nitrogen gas. The temperature was monitored throughout the illumination period with a copper–constantan thermocouple. The S_2-ann. samples were generated by warming (annealing) the S_2-$g4$ samples to 195 K in the dark for 90 s and then freezing in liquid nitrogen within 2 s.

Low-temperature X-band EPR spectra were recorded using a Varian E109 EPR spectrometer equipped with a Model 102 microwave bridge. Sample temperature was maintained at 8 K using an Air Products LTR liquid helium cryostat. Spectrometer conditions were as follows: microwave frequency, 9.21 GHz; field modulation amplitude, 3.2 mT at 100 kHz; microwave power, 30 mW. EPR MLS amplitudes were quantitated by adding the peak-to-trough amplitudes of four of the downfield and two of the upfield hyperfine lines, relative to $g = 2$.

The amount of Q_A^- signal from each EPR spectrum was estimated by the following equation:

$$q' = b' - a'(b/a)$$

where b' is the peak-to-trough amplitude of an MLS hyperfine peak located at the Q_A^- region, and a' is the amplitude of a second MLS peak at field lower than the $g = 2$ region, where no Q_A^- or other EPR signal is present. b and a, measured from a flash-induced S_2 state, are the amplitudes of the two MLS hyperfine peaks located at the same magnetic field with respect to b' and a'. This flash-induced S_2 state was generated at room temperature using either a xenon lamp or a Nd-YAG laser. At room temperature, the electron transfer from Q_A

to Q_B is not blocked, and therefore no Q_A^- signal is produced. q' is the amplitude of Q_A^- before normalization. Both the MLS and Q_A^- (q) amplitudes were normalized to correct for variable sample concentrations and volume. All spectra were quantitated from the light-minus-dark difference spectra.

X-ray Absorption Measurements. X-ray absorption K-edge spectra were collected at beam line VII-3, and EXAFS spectra were collected at beam lines IV-2 and VI-2 at the Stanford Synchrotron Radiation Laboratory (SSRL); some EXAFS spectra were collected on beam line X9-A at the National Synchrotron Light Source (NSLS). Si⟨220⟩ double-crystal monochromators were used for all of the X-ray absorption measurements. The second crystal was detuned to 75% of the maximum flux to reduce the flux of the X-ray harmonics. All samples were maintained at 10 ± 1 K in an Oxford liquid helium cryostat. To ensure sample integrity, EPR spectra were recorded before and after X-ray measurements.

X-ray absorption spectra were collected in the fluorescence mode (Jaklevic et al., 1977), using a Canberra Industries 13-element Ge solid-state detector as previously described (Cramer et al., 1988; DeRose, 1990). The fluorescence signal was recorded by setting the single-channel analyzer window of each Ge element to the Mn Kα peak. In most cases, total count rates on the outer Ge elements were limited to less than 40 kHz, and the amplifier shaping time was 0.5 μs. For the inner elements, the total count rates during the measurements were maintained at less than 30 kHz, and the amplifier shaping time was 0.75 μs. For the central Ge element, the total count rate was no more than 19 kHz, and the shaping time was 1 μs.

An unfocused X-ray beam, with about 1-eV energy resolution, was used for edge studies. Energy calibration was maintained by simultaneously measuring the narrow "white line" feature of $KMnO_4$ at 6543.3 eV. The slit in front of the I_0 detector was closed to a vertical size of 1 mm. The full width at half-maximum of the $KMnO_4$ white line was 1.6 ± 0.1 eV. Typical edge spectra were recorded by scanning from about 40 eV below to 50 eV above the edge. The point density was 5 points/eV. Each spectrum contained 401 points and required about 20 min to collect. At least five edge scans were averaged for each sample. Each EXAFS spectrum contained 344 points, with higher point density around the pre-edge region (0.25 eV/point) for better $KMnO_4$ energy referencing. Typical scans were collected from 150 eV below to 560 eV above the edge and required about 40 min.

The inflection energies in this article were obtained from the zero-crossing points of the second derivatives generated by analytical differentiation of a third-order polynomial fit to the data over an interval of ±3.0 eV on each side of a data point. The uncertainty in the inflection point energy is ±0.1 eV. The values of these inflection point energies are different from those previously reported by our group. This is due to the methods used to obtain those values. In our earlier studies, we used the maxima of the first derivatives obtained from a second-order polynomial sliding fit to the edge spectra (Yachandra et al., 1987; Cole et al., 1987; Guiles et al., 1990a,b).

X-ray Data Analysis. The data were analyzed as described in detail elsewhere (Yachandra et al., 1987; Guiles et al., 1990a,b; DeRose, 1990). A brief outline follows. The EXAFS modulation of the absorption $\chi(k)$ is described by the following equation:

$$\chi(k) = \sum_j \left[\frac{N_j |f_j(k,\pi)|}{kR_j^2} e^{-2\sigma_j^2 k^2} \sin[2kR_j + \alpha_j(k)] \right]$$

where N_j is the number of back-scattering neighbors of type j for a given absorber atom (Mn) at a distance R_j, $|f_j(k,\pi)|$ is the back-scattering amplitude of the jth atom and is a function of the atomic number of the back-scattering element, k is the magnitude of the photoelectron wave vector given by $k = [(2m_e/h^2)(E - E_0)]^{1/2}$, where m_e is the electron mass, E is the X-ray photon energy, E_0 is the threshold photoionization energy, and h is Planck's constant. The function α_j includes the phase shift of the absorber–back-scatterer pair. The Debye–Waller factor σ describes the attenuating effect resulting from thermal and static disorder.

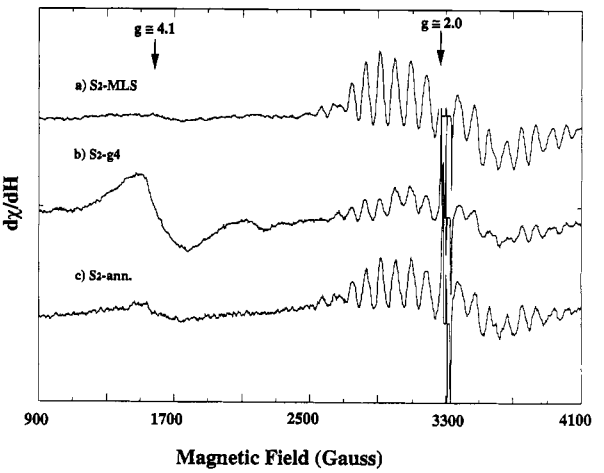

FIGURE 1: Illuminated-minus-dark difference EPR spectra of PSII samples from spinach in the (a) S_2-MLS state, (b) S_2-$g4$ state, and (c) S_2-ann. state. Spectrometer conditions are described under Materials and Methods.

The Mn EXAFS data from PSII samples were fit with theoretical values for the back-scattering amplitude and phase shifts for the scattering–absorbing pairs, on the basis of the curved-wave formalism of McKale et al. (1988). In this work, the Debye–Waller parameters were allowed to vary over a range comparable to that derived from multinuclear Mn compounds. The energy of the absorption edge (E_0) was varied in simulations to allow better phase matching to the experimental waves. The parameter E was allowed to change ±20 eV from E_0, which was the energy at maximum peak height of the Mn K-edge. The values of the average distance R_j, the number of scattering atoms N_j at distance R_j, the Debye–Waller factor σ_j, and the threshold energy E_0 were simultaneously fit with a nonlinear least-squares fitting program (Goodin, 1983; Guiles, 1988).

RESULTS

EPR Spectroscopy. Figure 1 shows the light-minus-dark EPR difference spectra of the S_2-MLS, S_2-$g4$, and S_2-ann. samples. Four light-induced features are seen in the S_2-$g4$ spectrum: a broad Q_A^- signal at $g \cong 1.9$, a small MLS centered about $g = 2$, a small peak at $g \cong 3.1$ representing the g_z feature of oxidized cytochrome b_{559}, and a broad $g \approx 4$ signal. Compared with the MLS amplitude of the S_2-MLS samples, the amount of MLS left in the S_2-$g4$ samples was approximately 20 ± 10%. After the S_2-$g4$ samples were annealed at 195 K in the dark for 90 s, the $g \approx 4$ signal typically disappeared, and the amount of MLS recovered to approximately 70%. The MLS could be restored to 100% after reillumination of these S_2-ann. samples at 195 K for 7 min. This indicated that up to 30% of the PSII centers were in the S_1 state after the annealing process. We believe, however, that most of these centers were not in the S_1 state in the S_2-$g4$ samples before the annealing process. The evidence is as follows.

(1) The amount of the Q_A^- signal generated in the S_2-$g4$ samples is approximately the same as that in the S_2-MLS

Table 1: Amplitudes of the Multiline and Q_A^- Signals of PSII Preparations

sample	MLS amplitude[a]	Q_A^- signal amplitude[b]
S_2-MLS	100%	6.4
S_2-*g*4	20%	6.6
S_2-ann.	70%	4.6
200 K illumination of the S_2-ann. samples	100%	6.7

[a] Multiline signal amplitudes are expressed as percentages of those of the S_2-MLS samples. Uncertainties in the MLS amplitude quantitation are ±10%. [b] Q_A^- signal amplitude is expressed as described in Materials and Methods. Uncertainties in the quantitation are estimated to be ±20%. Variations among samples are within 6%.

samples (Table 1, see Materials and Methods for the quantitation of the Q_A^- signal). At temperatures below 195 K, electron transfer from Q_A to Q_B is blocked. Therefore, the amount of Q_A^- accumulated is equal to the amount of the advancement from the S_1 to S_2 state. This indicates that the amount of the PSII reaction center in the S_2 state is approximately the same for the S_2-*g*4 and S_2-MLS states.

(2) The amount of Q_A^- signal decreased by approximately 30% in the S_2-ann. samples after annealing of the S_2-*g*4 samples (Table 1). This is consistent with 30–40% Q_A^- radical recombination with the S_2 state to form the S_1 state, resulting in only 60–70% MLS recovery after the annealing process.

(3) Cytochrome b_{559} can function as an alternative electron donor to the PSII reaction center. Although a small oxidized cytochrome signal was detected in some of our untreated S_2-*g*4 samples, the same EPR and EXAFS results were obtained from the S_2-*g*4 samples generated from the S_1 state, which did not contain any oxidizable cytochrome b_{559} in the PSII. These samples were prepared by treating the PSII with octacyanotungstate(V) before being dark-adapted. Octacyanotungstate(V), with its high reduction potential, has been used to oxidize cytochromes in PSII (Casey & Sauer, 1984).

The PSII centers in the S_2-*g*4 state have been reported to be less stable than those in the S_2-MLS state. Approximately 20% of the PSII centers in the S_2-*g*4 state was shown to recombine with Q_A^-, generating the S_1 state at 220 K (Zimmermann & Rutherford, 1986). Our EPR results showed a decrease of approximately 30 ± 10% of the Q_A^- signal in the S_2-ann. samples. The difference in the percentage may be due to the uncertainty in the Q_A^- amplitude quantitation.

Mn K-Edge Spectra. The Mn K-edge absorption spectra and the edge inflection energies of the representative S_1, S_2-*g*4, and S_2-MLS samples are compared in Figure 2a. All samples contain a pre-edge 1s→3d transition at approximately 6541 eV, which becomes allowed in a coordination environment that is not centrosymmetric. A shift in the absorption edge to energy higher than that of the S_1 state is apparent in the S_2-*g*4, S_2-MLS, and S_2-ann. (not shown) samples, with increases of 0.8, 1.1, and 0.9 eV, respectively. The edge inflection energies of the S_2-*g*4 and S_2-ann. samples are, respectively, 0.3 and 0.2 eV lower than that of the S_2-MLS sample.

Moreover, the edge shape of the S_2-*g*4 samples is clearly different from that of the S_2-MLS samples at the region close to the top of the edge (marked with arrows). Figure 2b shows the corresponding second derivatives of the K-edge spectra from Figure 2a. The second derivatives reveal reproducible changes of features among the S_1, S_2-*g*4, and S_2-MLS samples. Feature X is minimal in the S_1 state, larger in the S_2-*g*4 state, and further increased in the S_2-MLS state. Features Z and Y are distinctive between the S_1 and S_2 states, but quite similar

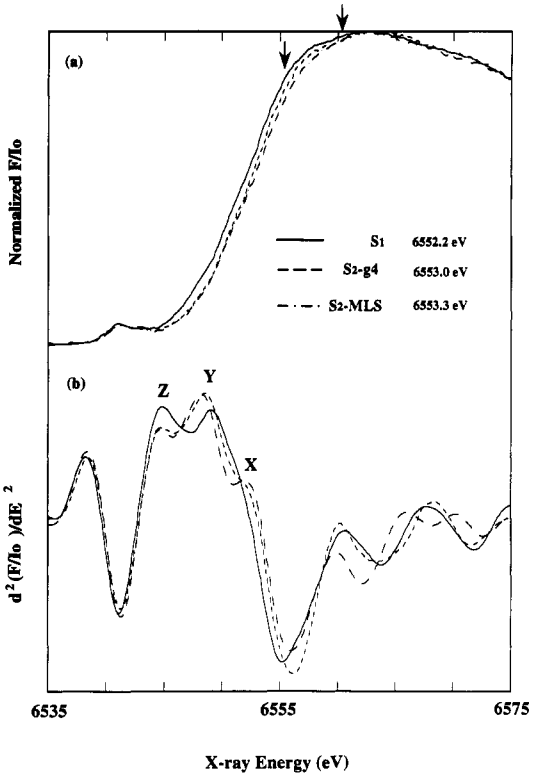

FIGURE 2: (a) Mn K-edge absorption spectra and inflection point energies of PSII particles from spinach poised in the S_1 (—), S_2-*g*4 (- - -), and S_2-MLS (– · –) states. (b) The corresponding second derivatives. A linear fit to the spectra below the Mn absorption edge has been removed. The inflection energies were obtained from the zero-crossing points of the second derivatives generated by analytical differentiation of a third-order polynomial fit to the data over an interval of ±3.0 eV on each side of a data point. The spectra were collected in the fluorescence mode and ratioed to the incident X-ray photon intensity, I_0. The inflection energy of the S_2-ann. samples (not shown) is 6553.1 eV.

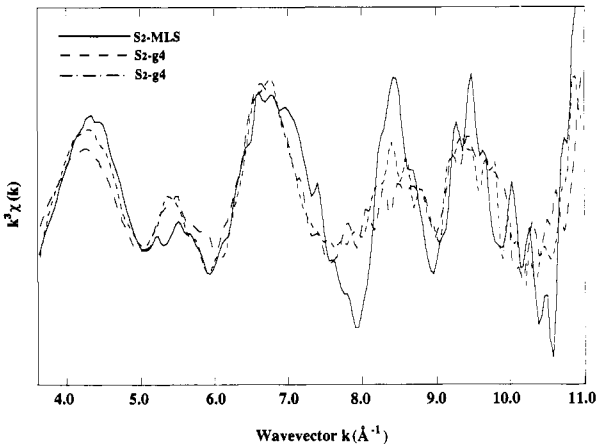

FIGURE 3: k^3-weighted EXAFS spectra of two kinds of S_2 samples: S_2-MLS (—) and two S_2-*g*4 samples (- - - and – · –).

within the two types of S_2 state. The small changes in edge position and shape are suggestive of a change in the structure of the Mn cluster of the S_2-*g*4 samples relative to those of either the S_2-ann. or S_2-MLS samples. The lower edge inflection energy of the S_2-ann. sample may result from an S_1 state (≅30%) fraction generated from recombination of the S_2-*g*4 centers with Q_A^- during the annealing process.

Mn EXAFS. The k^3-weighted EXAFS spectra of representative S_2-MLS and S_2-*g*4 samples show reproducible differences in the region of k = 8–10 Å^{-1} (Figure 3). The Fourier transforms of the k^3-weighted Mn EXAFS of the S_1 and S_2-MLS samples are shown in Figure 4. In Figure 4, the

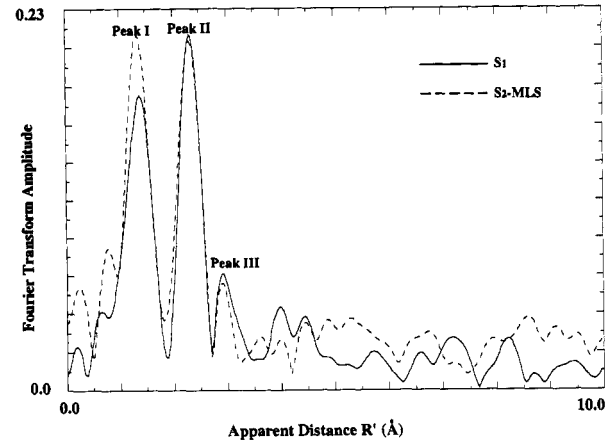

FIGURE 4: Fourier transform spectra of the k^3-weighted Mn EXAFS of the S_1 (—) and S_2-MLS states (- - -). The distances indicated are shorter than the actual distances to the scattering shells because of an average phase shift that is characteristic of the given absorber–scatterer pair.

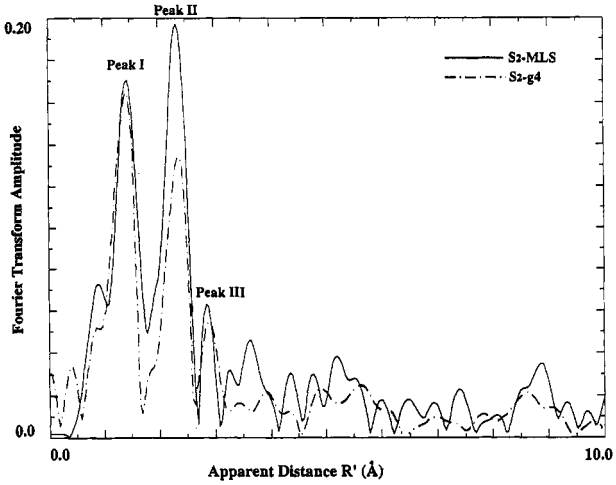

FIGURE 5: Fourier transform spectra of the k^3-weighted Mn EXAFS of the S_2-$g4$ sample (- · -) and the S_2-MLS sample (—). The significantly smaller peak II in the EXAFS of the S_2-$g4$ sample indicates a more disordered system. The amplitude decrease in peak III is less prominent than that in peak II.

positions of the three peaks, labeled peaks I–III, correspond to the shells of scatterers at different "apparent" distances from a Mn absorber. These apparent distances are shorter than the actual distances due to an average phase shift induced by the potential effect of the given absorber–scatterer pair on the photoelectron (Sayers et al., 1971). Peaks II and III are quite similar between the S_1 and S_2-MLS states (Figure 4). Peak I in Figure 4 is assigned to 2 ± 0.2 N or O ligand atoms at a distance of ~1.8 Å and 2–4 N or O ligand atoms at distances between 1.95 and 2.15 Å. Peak II is mainly due to the back-scattering from 1.2 ± 0.2 Mn neighbors at 2.7 Å from the Mn absorber. Peak III could arise from Mn or Ca at about 3.3 Å (Sauer et al., 1992; Yachandra et al., 1993).

The Fourier transform spectra (Figure 5) of the S_2-$g4$ sample k-space data (Figure 3) show that peaks II and III are decreased in amplitude relative to the S_2-MLS samples. The amplitude decrease of peak III is less prominent than that of peak II. The heights of these major Fourier transform peaks for the S_2-$g4$, S_2-MLS, S_1, and S_2-ann. samples are listed in Table 2. The heights of peaks II and III of the S_2-$g4$ samples are, respectively, 60 ± 10% and 75 ± 10% of the corresponding peaks of the S_2-MLS and S_1 samples. After the S_2-$g4$ samples were annealed to 195 K in the dark for 90 s, the amplitudes of peaks II and III recovered to 90–95% and 100%, respectively.

Table 2: Relative Peak Heights of the Fourier Transform of the EXAFS Data from the S_2-$g4$, S_2-MLS, S_2-ann., and S_1 Samples[a]

sample	peak I	peak II	peak III
S_1	0.18	0.21	0.07
S_2-$g4$[b]	0.18	0.12	0.05
S_2-MLS[c]	0.20	0.20	0.07
S_2-ann.[c]	0.19	0.19	0.08

[a] Peak heights are normalized to the edge jump. [b] Average results obtained from four samples; the uncertainty within these samples is estimated to be ±0.05 in peak I, ±0.02 in peak II, and ±0.01 in peak III of the average values in this table. [c] Average values from two samples with an uncertainty of ±8% in peak I and ±1% in peak II or peak III.

To determine whether the decreases in the Fourier transform peak heights were a result of sample damage caused by X-ray exposure, an S_2-$g4$ sample was annealed to 200 K after the XAS experiment. The intensity of the MLS recovery for this test sample was the same as that obtained from the annealed samples before the XAS experiment. Further evidence against the occurrence of X-ray damage was provided by the Mn K-edge spectra of the S_2-$g4$ samples. It has been reported that damage to the Mn cluster of the OEC results in a release of Mn^{2+}, which shows a sharp characteristic feature in the Mn K-edge spectra of the PSII samples (Cole et al., 1987). Our samples did not show such a Mn^{2+} feature.

Curve Fitting of Peak II. Peak II in the Fourier transform spectra of the S_2-$g4$ samples is substantially smaller than that of the S_2-MLS samples. This decreased amplitude is characteristic of an increased distance disorder. To further assess the relation between the amplitude decreases in the Fourier transform peaks and the possible structural changes in the Mn clusters in the OEC, each isolated R-space peak was back-transformed to k-space. Simulations using the curved-wave approximations were then performed on these isolated k-space data (McKale et al., 1988).

The Fourier-isolated k-space spectra, reflecting back-scattering from the second coordination shell of the Mn cluster in the S_2-$g4$ and S_2-MLS samples, together with their simulated k-space spectra are shown in Figure 6. On the basis of the EXAFS analysis on the S_1 and S_2-MLS samples (McDermott et al., 1988; DeRose, 1990), it is estimated that there is 1.2 ± 0.2 Mn–Mn vectors at 2.7 Å from each Mn absorber. However, single-shell fits to peak II from the S_2-$g4$ samples with the Mn coordination number constrained to 1.2 result in least-squares residuals 2–10-fold larger than those from the two subshell fits (Table 3). In addition, the Debye–Waller factors for these single-shell fits are 2–4-fold larger than the values (about 0.005 Å^2) reported previously (Yachandra et al., 1993) (Table 3). Fits to the second shell EXAFS of the S_2-$g4$ samples with an unconstrained Mn coordination number also produced unsatisfactory fitting results, including (1) at least a 4-fold increase of the least-squares residuals, (2) a doubling of the values of the Mn–Mn Debye–Waller factors, and (3) only 0.65 Mn–Mn vector in this shell (data not shown). The results described above indicate that peak II of the S_2-$g4$ state corresponds to more than one subshell.

Our previous EXAFS study on the F^--treated S_2 state also required two subshells ~2.7 Å from the Mn absorber (DeRose, 1990). Therefore, a series of simulations and fits was made for a model with two subshells on the S_2-$g4$ samples (Table 4). The numbers of scatterers of the two subshells were allowed to vary but their sum was fixed to a value of 1.2, which was obtained from our previous study of the S_1 and S_2-MLS states (McDermott et al., 1988; DeRose, 1990). The resulting least-squares residuals decreased to one-quarter of those from the one-shell fits. In addition, the two-shell fits provide more

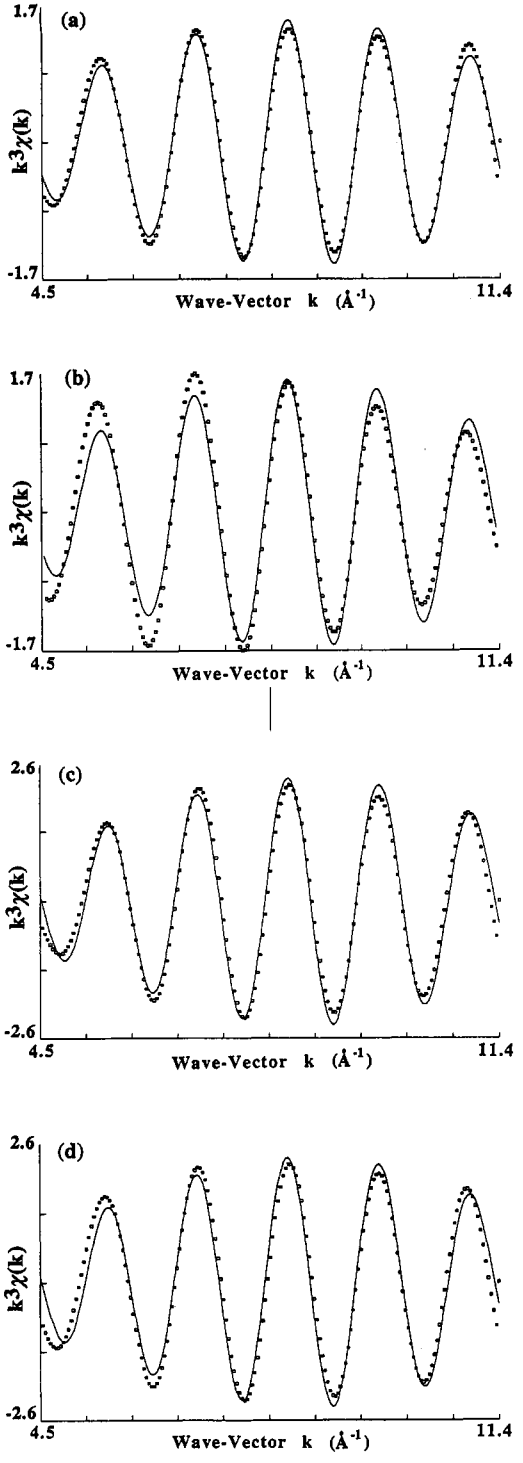

FIGURE 6: *k*-space spectra of isolated peak II (—) for the S_2-*g*4 and S_2-MLS samples. These EXAFS oscillations were obtained by first applying a window function to peak II and then back-transforming it to *k*-space. The fit to a Fourier-isolated peak II is indicated by the □ traces. The spectra shown are of (a) the S_2-*g*4 sample simulated with two Mn subshells, (b) the S_2-*g*4 sample simulated with one Mn shell, (c) the S_2-MLS sample simulated with two Mn subshells, and (d) the S_2-MLS sample simulated with one Mn shell. Simulation parameters for the fits are listed in Table 4. Inclusion of a second subshell is shown to be important for improving the quality of the fits for the S_2-*g*4 samples. Much less improvement is obtained with the fits of the S_2-MLS samples.

reasonable values of the Debye–Waller factor for each subshell and much better fit quality (see Figure 6a,b).

In contrast, when two-subshell fits to the EXAFS data from the S_1, S_2-MLS, and S_2-ann. samples are performed, 2–10-fold larger Debye–Waller factors are found in at least one of the two subshells, which is contrary to what is expected (Table 4). When the fitting included two Mn subshells with unconstrained coordination numbers, the 2.74-Å subshell accounts for nearly 90% of the total second shell scatterers (data not shown). For some samples, good two-shell fits are observed with two close subshells (2.72 and 2.77 Å). All of these facts indicate that a two-subshell model is not necessary for the S_1, S_2-MLS, and S_2-ann. samples.

Table 3: One-Shell Simulation Results for the Second Shell of the k^3-Weighted EXAFS Data of the S_2-*g*4 Samples

sample[c]	N^a	R (Å)	$2\sigma^2$ (Å²)	ΔE_0	F^b
1	1.2	2.74	0.011	−16.0	20[d]
2	1.2	2.72	0.011	−17.6	11[d]
3	1.2	2.80	0.020	−11.5	9[d]
4	1.2	2.73	0.010	−16.0	7

[a] The coordination number, *N*, was constrained to 1.2. [b] *F* is the least-squares residual difference between the Fourier-isolated EXAFS and the EXAFS calculated by using theoretical phase and amplitude functions using curved-wave approximations. [c] Four individual S_2-*g*4 samples.[d] The differences between the fits and the experimental traces are large.

Table 4: Simulation Results for the Second Shell of the S_2-*g*4, S_2-MLS, S_1, and S_2-ann. Samples

(A) One-Shell Fits for k^3-Weighted Data

	N^b	R (Å)	$2\sigma^2$ (Å²)	ΔE_0	F
S_2-*g*4[a]	1.2	2.73	0.010	−17.0	8
S_2-MLS	1.2	2.73	0.005	−14.1	13
S_2-ann.	1.0	2.72	0.004	−18.0	10
S_1	1.2	2.74	0.006	−13.7	6

(B) Two-Shell Fits for k^3-Weighted Data

	N_1[b]	R_1 (Å)	$2\sigma^2$ (Å²)	ΔE_0	N_2	R_2 (Å)	$2\sigma^2$ (Å²)	ΔE_0	F
S_2-*g*4[a]	0.76	2.72	0.001	−13.0	0.44	2.85	0.003	−19.20	2
S_2-MLS	0.6	2.71	0.002	−19.9	0.60	2.81	0.012	0.35	9
S_2-ann.	0.6	2.71	0.010	−19.0	0.60	2.90	0.040	7.00	9
S_1	0.6	2.72	0.003	−18.7	0.60	2.87	0.020	4.11	3

[a] Average results were obtained from the four S_2-*g*4 samples in Table 3. In general, distances obtained for individual samples differed by less than 0.02 Å. [b] The number of scatterers determined at a given distance in different samples of each type was found to be within 8%.

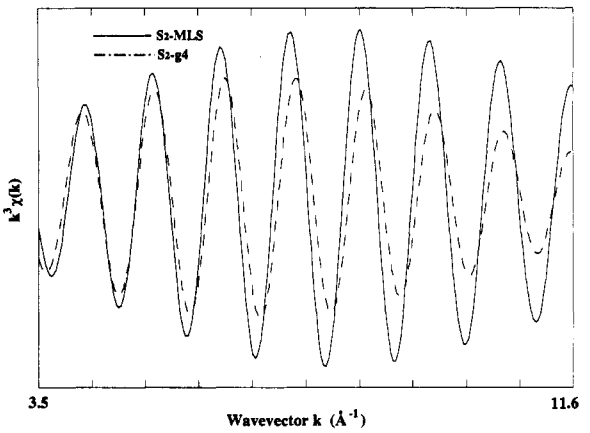

FIGURE 7: Fourier isolates to the third shell of the k^3-weighted Mn EXAFS of the S_2-*g*4 sample (– · –) and the S_2-MLS sample (—).

Curve Fitting to Peak III. Curve fitting of peak III was performed on isolated, back-transformed *k*-space spectra, as was done for peak II. The isolated *k*-space oscillations of the S_2-*g*4 samples have a lower overall amplitude and are damped at higher *k*-values in comparison with the S_2-MLS samples (Figure 7). This indicates greater distance disorder in this shell of the S_2-*g*4 samples and is consistent with the smaller amplitude of peak III in the Fourier transform spectra. The simulation results are summarized as follows.

(1) S_2-g4 Samples. Peak III can be fit to a single Mn shell (denoted the 1-Mn fits) at 3.35 Å with an unconstrained

Table 5: Simulation Results for the Third Coordination Shell of the S_2-g4, S_2-MLS, S_1, and S_2-ann. Samples with k^3-Weighted EXAFS Data[a]

(A) One-Shell Fits for k^3-Weighted Data (1-Mn Fits)

	N	R (Å)	$2\sigma^2$ (Å^2)	ΔE_0	F[b]
S_2-g4	0.72	3.35	0.014	−11.4	0.41
S_2-MLS	0.40	3.31	0.007	−13.5	0.47
S_2-ann.	0.48	3.30	0.005	−20.0	1.08
S_1	0.48	3.31	0.005	−13.1	0.77

(B) Two-Shell Fits for k^3-Weighted Data from S_2-g4 Samples

		N	R (Å)	$2\sigma^2$ (Å^2)	ΔE_0	F[b]
2-Mn_a fits	Mn_1	0.60	3.33	0.0025	−4.4	0.13
	Mn_2	0.56	3.45	0.0043	−11.2	
2-Mn_b fits	Mn_1	0.40	3.33	0.0034	−7.2	0.15
	Mn_2	0.20	3.47	0.0044	−1.7	
Mn+Ca fits	Mn	0.50	3.35	0.0045	−4.3	0.13
	Ca	0.26	3.55	0.0012	−4.0	

[a] In general, distances obtained for individual samples differed by less than 0.02 Å. The number of scatterers determined at a given distance was found to be within 20%. [b] F is the least-squares difference between the Fourier-isolated EXAFS and the EXAFS calculated by using theoretically derived phase and amplitude functions with curved-wave formalism (McKale et al., 1988).

Debye–Waller factor (0.014 Å^2). The 1-Mn fits to the S_2-g4 samples also require a coordination number larger than that for the S_2-MLS, S_2-ann., or S_1 samples (Table 5A). This larger coordination number is suggestive of a larger Mn scatterer contribution and indicates the possibility of an additional Mn–Mn vector at ~3 Å.

Satisfactory fitting results are also found in three types of two-subshell fits (Table 5B): (a) the 2-Mn_a fits, with 1.2 ± 0.1 Mn–Mn vectors; (b) the 2-Mn_b fits, with 0.6 ± 0.05 Mn–Mn vector; and (c) the Mn+Ca fits, with 0.5–0.6 Mn–Mn vector and 0.26–0.3 Mn–Ca vector per Mn atom in the cluster. All of the two-subshell fits reduce the least-squares residuals up to 3-fold and the Debye–Waller factors of each subshell approximately 3–10-fold. The first subshell in these three types of fits is approximately 3.33 Å from the Mn absorber. The second subshell is about 0.11 Å (the 2-Mn_a and 2-Mn_b fits) or 0.20 Å (the Mn+Ca fits) more distant than the first subshell.

For the 2-Mn_a fits, the coordination number is distributed equally between the two subshells and is approximately twice the value reported in our previous studies (DeRose, 1990; Yachandra et al., 1993). For the 2-Mn_b fits, the distribution of the 0.6 Mn–Mn vector is uneven, with the ratio of the coordination numbers between the two subshells ranging from 1.5:1 to 2:1. The back-scatterer of the second subshell is replaced by a calcium in the Mn+Ca fits. The Mn+Ca fits are obtained by constraining the coordination number of each subshell to a physically meaningful value (Table 5B). The distance of the Ca subshell from the Mn+Ca fits is approximately 0.1 Å farther than that of the second subshell in the 2-Mn_a and 2-Mn_b fits. As the fit quality among the 2-Mn_a, 2-Mn_b, and Mn+Ca fits is similar, we cannot exclude any of the two subshell fits for peak III on the basis of the present data.

(2) S_2-MLS, S_2-ann., and S_1 Samples. Satisfactory results are obtained from the 1-Mn fits in these samples (Table 5A). The fits to two Mn subshells result in large Debye–Waller factors from each subshell and therefore are unnecessary (data not shown). However, a Mn+Ca fit results in a decrease in both the Debye–Waller factors from both subshells and the least-squares residuals relative to those of the 1-Mn fits. Therefore, we could not exclude the possibility of the Mn+Ca fits to the third shell. The coordination numbers and distances from the best fits for these samples are similar to those from the Mn+Ca fits of the S_2-g4 samples (Table 5B).

Table 6: Effective Subshell Coordination Numbers (N_1 and N_2) Based on EPR Measurements and on EXAFS Data from Four Individual S_2-g4 Samples ($N_1 + N_2 = 1.2$)

% of residual MLS from EPR	N_1, N_2 estimated using % of residual MLS from EPR	N_1, N_2 from the best EXAFS fits
sample 1, 23	0.74, 0.46	0.76, 0.44
sample 2, 22	0.73, 0.47	0.76, 0.44
sample 3, 19	0.71, 0.49	0.68, 0.52
sample 4, 21	0.72, 0.48	0.72, 0.48

DISCUSSION

Edges. Our Mn K-edges from the S_2-g4 samples showed an edge shift of 0.8 eV to higher energy after the S_1 samples were illuminated at 131 K. This result, which indicated that Mn is oxidized during the S_1 to S_2-g4 transition, is in agreement with the previous edge study for samples measured at 170 K (Cole et al., 1987). Our present data, with improved signal-to-noise, showed subtle differences in the edge shape and inflection energy from the previous report. Analyses of the second derivatives of the K-edge spectra further revealed reproducible changes in features between the S_2-g4 and S_2-MLS samples. A structural change within the Mn cluster could be responsible for this change in edge shape, and this possibility is supported by the EXAFS data (below).

EXAFS Studies on Peak II of the S_2-g4 State. In the present study, the best simulations of peak II were obtained by introducing two Mn–Mn subshells. One subshell is at 2.72 Å, which is close to that found for the S_2-MLS and S_1 states. The other subshell is at 2.85 Å. Upon annealing, the distance of this subshell changes back to ~2.72 Å again. The Mn–Mn distance in μ-oxo-bridged compounds depends on both the bridging Mn–oxo distance and the Mn–oxo–Mn bond angle. It has been shown that, in a synthetic model compound, the oxidation of Mn(III,IV) to Mn(IV,IV) causes an increase in the Mn–Mn distance of 0.05 Å (Wieghardt, 1989). The distance increase could be even larger in a protein environment where ligands are derived from amino acid side chains (DeRose, 1990).

Other than the S_2-g4 samples, our previous report on the S_3 state also showed inhomogeneity in its peak II (Guiles et al., 1990b). In addition, the Fourier transform of the EXAFS data obtained from annealed ammonia-treated S_2 states also shows a smaller peak II (Dau et al., manuscript in preparation). However, there are differences between the S_2-g4 and both the ammonia-treated and S_3 samples. In the case of the ammonia-treated and S_3 samples, the second peak could be fit by increasing the Debye–Waller factor. In the case of the S_2-g4 data, it is clear that two different distances are required; just increasing the Debye–Waller parameter does not lead to a satisfactory fit. This fact implies that the second shell disorder of the S_2-g4 state is probably larger than that of the S_3 state or the ammonia-treated S_2 state.

The best two-shell fits obtained for peak II of the S_2-g4 samples give inequivalent values for the coordination numbers of Mn scatterers for each subshell. Approximately 60% of the total scatterers is contributed by the 2.72-Å subshell and 40% by the 2.85-Å subshell (see Table 4). We propose that 40% of the 2.72-Å vector arises from the S_2-g4 state, which contains equal amounts of the 2.72- and 2.85-Å vectors. The additional 20% of the 2.72-Å vector is contributed by a fraction of the sample responsible for the small S_2-MLS residuals in the S_2-g4 sample. This argument is supported by our EPR measurements. Table 6 shows that the coordination

numbers of the two subshells estimated from the S_2-*g*4 samples are close to those obtained from the best fits of our EXAFS data.

EXAFS Studies on Peak III of the S_2-g4 State. To fit peak III of the Fourier transforms from the PSII samples is more challenging due to its small amplitude. The backscattering contribution is weaker and more complicated at this longer distance. Relative to the S_2-MLS, S_2-ann., or S_1 samples, the S_2-*g*4 samples contain an increased distance disorder in peak III, which results in a larger Debye–Waller factor required for the one-shell fits. Three possible two-subshell fits were also investigated: (a) the 2-Mn_a fits, (b) the 2-Mn_b fits, and (c) the Mn+Ca fits. Among these simulation results, the 1-Mn and Mn+Ca fits are compatible with the model of the Mn complex previously proposed by our group (Yachandra et al., 1993). However, to satisfy the 2-Mn_a fits would require an additional Mn–Mn vector at ~3.45 Å in the S_2-*g*4 state, and this would imply a large structural rearrangement in the Mn cluster. Further, the possible interpretation of the 2-Mn_b fits requires heterogeneity in the PSII centers, where two-thirds of the centers contain 0.6 Mn–Mn vector at 3.33 Å and the other one-third at 3.47 Å.

On the other hand, the best fits to peak III of the S_2-MLS, S_2-ann., or S_1 samples for the 1-Mn or Mn+Ca fits require only one distance and 0.5 Mn–Mn vector per Mn atom in the cluster. The 1-Mn and Mn+Ca fits are indistinguishable, and this is consistent with the previous results from the S_2-MLS or S_1 PSII samples prepared from either spinach or cyanobacteria (DeRose, 1990).

It has been reported that the EXAFS curve-fitting techniques are problematic in dilute biological samples when attempting to identify scattering atoms at distances >3 Å, and hence it is difficult to arrive at a unique structural solution from such fits (Scott & Eidsness, 1988). Our results for peak III also do not provide a unique solution for the S_1, S_2-*g*4, S_2-ann., or S_2-MLS samples. The ambiguity of differentiating among various fits to peak III indicates that other approaches are required to reveal its composition. It has been shown that, for the Ca^{2+}-depleted PSII particles, the oxygen-evolving activity can be revived by adding Sr^{2+}, which is believed to replace the Ca^{2+} (Boussac & Rutherford, 1988). Therefore, fits of peak III from the Fourier transform spectra of the Sr^{2+}-substituted PSII particles provide more direct evidence of a probable calcium scatterer. Previous studies in our group on the Sr^{2+}-reconstituted PSII strongly support the existence of Ca scatterers in peak III (Yachandra et al., 1993; Latimer et al., manuscript in preparation).

Models. In our previous report, we proposed a model for the Mn cluster on the basis of the EXAFS results of the S_1 and S_2-MLS states (DeRose, 1990; Yachandra et al., 1993). The overall structure of the Mn complex in the S_1 state is similar to that of the S_2-MLS state. As shown in Figure 8b, the Mn cluster in either of these states is proposed to consist of a pair of di-μ-oxo-bridged Mn dimers (labeled as dimers I and II) with a 2.7-Å Mn–Mn separation in each dimer. Mn_A in dimer I and Mn_C in dimer II, separated by ~3.3 Å, are linked by a mono-μ-oxo bridge and a mono-μ-carboxylato or di-μ-carboxylato bridge. The distances between the Mn_A–Mn_D, Mn_B–Mn_D, and Mn_B–Mn_C pairs are longer and are not detected in our EXAFS data. Note that this model is only one of the topologically equivalent possibilities that are compatible with our data. Detailed model candidates will be discussed elsewhere (DeRose et al., submitted for publication). In the S_2-MLS state, dimers I and II are proposed to be Mn(IV,IV) and Mn(III,IV), respectively, on the basis of our previous results from the Mn K-edge spectra. Two speculative

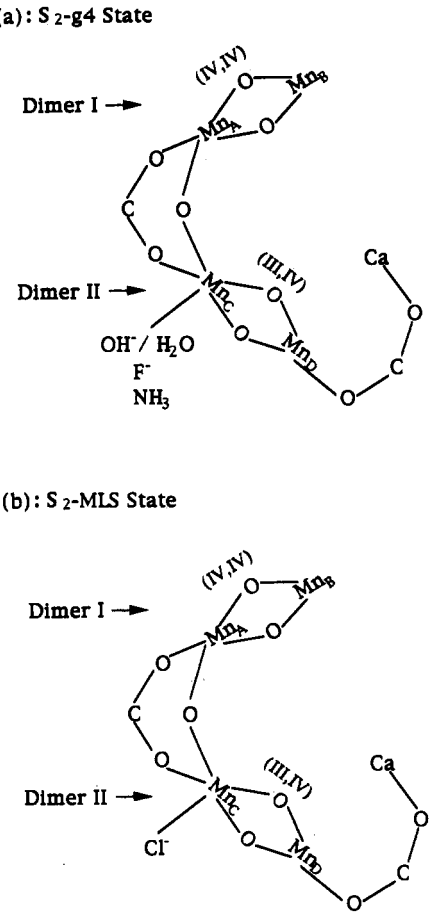

FIGURE 8: Structural model for (a) the S_2-*g*4 state and (b) the S_2-MLS state. Mn(IV,IV) and Mn(III,IV) are denoted by dimer I and dimer II, respectively. The S_2-*g*4 state is suggested to arise from the middle Kramers doublet of an $S = {}^5/_2$ spin state, which is generated by the ferromagnetic coupling between the dimer I ground state with $S_I = {}^1/_2$ and the dimer II second excited state with $S_{II} = 2$. In this model, a critical ligand site is occupied by an OH^-/H_2O ligand, which modulates the exchange coupling in the Mn complex. In the structure of the S_2-MLS state, chloride is allowed to occupy the critical site resulting from ligand rearrangement at 200 K. This rearrangement results in the $S = {}^1/_2$ ground state due to the antiferromagnetic coupling between $S_I = {}^1/_2$ and $S_{II} = 0$.

sites for the Cl^- and Ca^{2+} ions are also shown in this model.

A similar model is proposed for the S_2-*g*4 state, with the following modifications based on the present study: (1) the Mn_C–Mn_D separation in dimer II increases from 2.73 to 2.85 Å; (2) an OH^-/H_2O ligand occupies the site where Cl^- is bound in the S_2-MLS state. We propose that the $g = 4$ signal arises from ferromagnetic coupling between the dimer II $S_{II} = {}^1/_2$ ground state and the $S_I = 2$ state of dimer I. On the other hand, the MLS arises from antiferromagnetic coupling between the dimer II ground state and the dimer I ground state with $S_I = 0$. To account for the appearance of the $g = 4$ EPR signal generated at 130 K, we propose that one critical ligand site is occupied by an OH^-/H_2O ligand, which is replaced by Cl^- in the S_2-MLS state. This proposal is consistent with the result that the $g = 4$ signal in Cl^--depleted S_2-*g*4 samples is replaced by MLS upon adding Cl^- in the dark at 0 °C (Ono et al., 1986). This OH^-/H_2O ligand modifies the molecular arrangement of the Mn cluster in a way that results in an increase in one of the Mn–Mn distances to 2.85 Å and increased heterogeneity in the 3.3-Å vector. This could modulate the magnetic coupling and result in ferromagnetic exchange coupling between these two dimers. Fluoride and ammonia, which enhance the $g = 4$ signal in the S_2 state, are also proposed to occupy the same site as the

OH^-/H_2O ligand. On the basis of the result that NH_3 and F^- compete for a Cl^- site on Mn (Yocum, 1992), it has been suggested that the conversion of the S_2-g4 to the S_2-MLS state involves the binding of Cl^-, even at a temperature as low as 160 K (Beck & Brudvig, 1988; Rutherford et al., 1991, 1992). Upon warming to 200 K, chloride can then, by small structural rearrangement in the Mn complex, replace the OH^-/H_2O at this site to generate the MLS. At the same time, the Mn–Mn distance of dimer II changes from 2.85 to 2.73 Å.

The single μ-oxo bridge between the two dimers plays a key role in the conversion from the S_2-g4 to the S_2-MLS state. Studies of inorganic compounds have shown that the exchange coupling through a single μ-oxo bridge between two Mn atoms can vary from weakly ferromagnetic ($J > 0$) to antiferromagnetic ($J < 0$), depending on the terminal ligands (Wieghardt, 1989). Unlike the di-μ-oxo-bridged Mn dimers, which usually have strong antiferromagnetic exchange coupling ($J \ll 0$), the flexibility of this single μ-oxo bridge makes the Mn complex more sensitive to the changes in its environment. It has been reported that a small change, such as protonation of the bridging oxygen, is enough to switch between these two types of exchange coupling (Hagen et al., 1989). For the S_2-g4 state, the low formation temperature (130 K) may inhibit rearrangement of the ligands around the Mn atoms. Such rearrangement would be required for the MLS formation and may happen only at higher temperatures (~200 K).

CONCLUSIONS

The structure of the S_2-g4 state is unique; it is similar to neither the S_1 nor the S_2-MLS state. Evidence comes from the results of our X-ray absorption spectroscopy study.

(1) EXAFS analyses indicate that a structural rearrangement occurs during the S_1 to S_2-g4 transition at 130 K, which causes the Mn–Mn distance in one of the di-μ-oxo-bridged Mn dimers to increase from 2.73 to 2.85 Å. An S_2-MLS state generated either by direct illumination of the S_1 state or by annealing the S_2-g4 state at 200 K has only one distance (2.72 ± 0.01 Å) in the second shell of scatterers. This change is proposed to arise from a rearrangement of the Mn cluster due to a Cl^- ligand binding that is not allowed at 130 K.

(2) EXAFS analyses also indicate a larger distance disorder of the third shell for the S_2-g4 state. Two subshells, reflecting either the 2-Mn or the Mn+Ca fit, as well as the 1-Mn fit with a large Debye–Waller factor, generate satisfactory simulations to the third shell. On the other hand, a 1-Mn or Mn+Ca fit is better for the S_1, S_2-MLS, or S_2-ann. states.

(3) Both the S_2-g4 and S_2-MLS states show a positive K-edge shift from the S_1 state. The energy of the Mn K-edge for the S_2-g4 state is 0.3 eV lower than that of the S_2-MLS state. In addition, the edge shapes are different for these two forms of the S_2 state. These differences could arise from the structural variation discussed in the EXAFS results.

ACKNOWLEDGMENT

We are grateful to Dr. B. Hedman and the staff at SSRL and Dr. S. Khalid at NSLS for their assistance with the beam lines. We also thank Joy C. Andrews and Roehl Cinco for help with data collection.

REFERENCES

Andréasson, L.-E. (1990) in *Current Research in Photosynthesis* (Baltscheffsky, M., Ed.), Vol. I, pp 785–788, Kluwer, Dordrecht, The Netherlands.
Beck, W. F., & Brudvig, G. W. (1986) *Biochemistry 25*, 6479.
Beck, W. F., & Brudvig, G. W. (1988) *Chem. Scr. 28A*, 93.
Berthold, D. A., Babcock, G. T., & Yocum, C. F. (1981) *FEBS Lett. 134*, 231.
Boussac, A., & Rutherford, A. W. (1988) *Biochemistry 27*, 3476.
Britt, R. D., Lorigan, G. A., Sauer, K., & Klein, M. P. (1992) *Biochim. Biophys. Acta 1040*, 95.
Casey, J. L., & Sauer, K. (1984) *Biochim. Biophys. Acta 767*, 21.
Cole, J. L., Yachandra, V. K., McDermott, A. E., Guiles, R. D., Britt, R. D., Dexheimer, S. L., Sauer, K., & Klein, M. P. (1987) *Biochemistry 26*, 5967.
Cramer, S. P., Tench, O., Yocum, M., & George, G. N. (1988) *Nucl. Instrum. Methods A266*, 586.
Debus, R. J. (1992) *Biochim. Biophys. Acta 1102*, 269.
De Paula, J. C., Beck, W. F., Miller, A.-F., Wilson, R. B., & Brudvig, G. W. (1987) *J. Chem. Soc., Faraday Trans. 1 83*, 3635.
DeRose, V. J. (1990) Ph.D. Thesis, University of California at Berkeley, Lawrence Berkeley Laboratory Report LBL-30077.
Dismukes, G. C., & Siderer, Y. (1981) *Proc. Natl. Acad. Sci. U.S.A. 78*, 274.
Goodin, D. B. (1983) Ph.D. Thesis, University of California at Berkeley, Lawrence Berkeley Laboratory Report LBL-16901.
Goodin, D. B., Yachandra, V. K., Britt, R. D., Sauer, K., & Klein, M. P. (1984) *Biochim. Biophys. Acta 767*, 209.
Guiles, R. D. (1988) Ph.D. Thesis, University of California at Berkeley, Lawrence Berkeley Laboratory Report LBL-25186.
Guiles, R. D., Yachandra, V. K., McDermott, A. E., Cole, J. L., Dexheimer, S. L., Britt, R. D., Sauer, K., & Klein, M. P. (1990a) *Biochemistry 29*, 486.
Guiles, R. D., Zimmermann, J.-L., McDermott, A. E., Yachandra, V. K., Cole, J. L., Dexheimer, S. L., Britt, R. D., Wieghardt, K., Bossek, U., Sauer, K., & Klein, M. P. (1990b) *Biochemistry 29*, 471.
Haddy, A., & Vänngård, T. (1990) in *Current Research in Photosynthesis* (Baltscheffsky, M., Ed.) Vol. I, pp 753–756, Kluwer, Dordrecht, The Netherlands.
Haddy, A., Dunham, W. R., Sands, R. H., & Aasa, R. (1992) *Biochim. Biophys. Acta 1099*, 25.
Hagen, K. S., Westmoreland, T. D., Scott, M. J., & Armstrong, W. H. (1989) *J. Am. Chem. Soc. 111*, 1907.
Hansson, Ö., & Andréasson, L.-E. (1982) *Biochim. Biophys. Acta 679*, 261.
Hansson, Ö., Aasa, R., & Vänngård, T. (1987) *Biophys. J. 51*, 825.
Jaklevic, J., Kirby, J. A., Klein, M. P., Robertson, A. S., Brown, G. S., & Eisenberger, P. (1977) *Solid State Commun. 23*, 679.
Kim, D. H., Britt, R. D., Klein, M. P., & Sauer, K. (1990) *J. Am. Chem. Soc. 112*, 9389.
Kim, D. H., Britt, R. D., Klein, M. P., & Sauer, K. (1992) *Biochemistry 31*, 541.
Kok, B., Forbush, B., & McGloin, M. (1970) *Photochem. Photobiol. 11*, 457.
MacLachlan, D. J., Hallahan, B. J., Ruffle, S. V., Nugent, J. H. A., Evans, M. C. W., Strange, R. W., & Hasnain, S. S. (1992) *Biochem. J. 285*, 569.
McDermott, A. E., Yachandra, V. K., Guiles, R. D., Cole, J. L., Dexheimer, S. L., Britt, R. D., Sauer, K., & Klein, M. P. (1988) *Biochemistry 27*, 4021.
McKale, A. G., Veal, B. W., Paulikas, A. P., Chan, S.-K., & Knapp, G. S. (1988) *J. Am. Chem. Soc. 110*, 3763.
Ono, T.-A., & Inoue, Y. (1989) *Arch. Biochem. Biophys. 275*, 440.
Ono, T.-A., Zimmermann, J.-L., Inoue, Y., & Rutherford, A. W. (1986) *Biochim. Biophys. Acta 851*, 193.
Ono, T.-A., Nakayama, H., Gleiter, H., Inoue, Y., & Kawamori, A. (1987) *Arch. Biochem. Biophys. 256*, 618.
Penner-Hahn, J. E., Fronko, R. M., Pecoraro, V. L., Yocum, C. F., Betts, S. D., & Bowlby, N. R. (1990) *J. Am. Chem. Soc. 112*, 2549.
Rutherford, A. W. (1989) *Trends Biochem. Sci. 14*, 227–232.
Rutherford, A. W., Boussac, A., & Zimmermann, J.-L. (1991) *New J. Chem. 15*, 491.

Rutherford, A. W., Zimmermann, J.-L., & Boussac, A. (1992) in *The Photosystems: Structure, Function and Molecular Biology* (Barber, J., Ed.) pp 179–229, Elsevier B. V., Amsterdam.

Sauer, K., Yachandra, V. K., Britt, R. D., & Klein, M. P. (1992) in *Manganese Redox Enzymes* (Pecoraro, V. L., Ed.) pp 141–175, VCH Publishers, New York.

Sayers, D. E., Stern, E. A., & Lytle, F. W. (1971) *Phys. Rev. Lett. 27*, 1204.

Scott, R. A., & Eidsness, M. K. (1988) *Comments Inorg. Chem. 7*, 235.

Wieghardt, K. (1989) *Angew. Chem., Int. Ed. Engl. 28*, 1153.

Yachandra, V. K., Guiles, R. D., McDermott, A. E., Cole, J. L., Britt, R. D., Dexheimer, S. L., Sauer, K, & Klein, M. P. (1987) *Biochemistry 26*, 5974.

Yachandra, V. K., DeRose, V. J., Latimer, M. J., Mukerji, I., Sauer, K., & Klein, M. P. (1993) *Science 260*, 675.

Yocum, C. F. (1992) in *Manganese Redox Enzymes* (Pecoraro, V. L., Ed.) pp 71–83, VCH Publishers, New York.

Zimmermann, J.-L., & Rutherford, A. W. (1984) *Biochim. Biophys. Acta 767*, 160.

Zimmermann, J.-L., & Rutherford, A. W. (1986) *Biochemistry 25*, 4609.